

Growth and design strategies of organic dendritic networks

Giuseppe Ciccone¹ · Matteo Cucchi^{1,2} · Yanfei Gao¹ · Ankush Kumar³ · Lennart Maximilian Seifert^{1,4} · Anton Weissbach¹ · Hsin Tseng¹ · Hans Kleemann¹ · Fabien Alibart³ · Karl Leo¹

Received: 16 June 2022 / Accepted: 13 July 2022

Published online: 22 July 2022

© The Author(s) 2022 **OPEN**

Abstract

A new paradigm of electronic devices with bio-inspired features is aiming to mimic the brain's fundamental mechanisms to achieve recognition of very complex patterns and more efficient computational tasks. Networks of electropolymerized dendritic fibers are attracting much interest because of their ability to achieve advanced learning capabilities, form neural networks, and emulate synaptic and plastic processes typical of human neurons. Despite their potential for brain-inspired computation, the roles of the single parameters associated with the growth of the fiber are still unclear, and the intrinsic randomness governing the growth of the dendrites prevents the development of devices with stable and reproducible properties. In this manuscript, we provide a systematic study on the physical parameters influencing the growth, defining cause-effect relationships for direction, symmetry, thickness, and branching of the fibers. We build an electrochemical model of the phenomenon and we validate it *in silico* using Montecarlo simulations. This work shows the possibility of designing dendritic polymer fibers with controllable physical properties, providing a tool to engineer polymeric networks with desired neuromorphic features.

1 Introduction

Electropolymerization driven by alternated electrical signals has been recently proven to be an effective route to produce artificial synapses, hardware-based neural networks, and electronic devices with a variety of neuromorphic features [1–6]. The experimental setup is typically composed of metal electrodes separated by an electrolytic solution containing a monomer which, upon the application of a voltage higher than its oxidation potential, polymerizes and forms a conductive polymer (CP). Direct current (DC) polymerization has largely been used to cover metal pads with polymeric films [7] for enhancing the devices' electrochromic properties [8], for optimizing dye-synthesized solar cells [9], for enhanced sensing [10] and bioelectronics [11, 12], and evolvable circuitry [13, 14]. This DC electropolymerization results in closed films covering the electrodes. Conversely, dendritic networks are obtained using an AC signal. Here, the stochastic nature of the process can harm the stability of inorganic devices, like in the case of batteries [15], but it is especially useful for the fabrication of devices where non-linearity, stability in wet environment, and ease of processing are required, such as artificial synapses or organic electrochemical transistors (OECTs). Interesting demonstrations of synaptic processes

Supplementary Information The online version contains supplementary material available at <https://doi.org/10.1007/s43939-022-00028-0>.

✉ Karl Leo, karl.leo@tu-dresden.de | ¹Dresden Integrated Center for Applied Physics and Photonic Materials (IAPP) and Institute for Applied Physics, Technische Universität Dresden, 01062 Dresden, Germany. ²Ecole Polytechnique Fédérale de Lausanne (EPFL), Laboratory for Soft Bioelectronic Interfaces, Geneva, Switzerland. ³Université de Lille, Centrale Lille CNRS, Univ. Polytechnique Hauts-de-France, UMR 8520-IEMN, 59000 Lille, France. ⁴Department of Computer Science, University of Chicago, Chicago, IL 60637, USA.



such as Pavlovian conditioning [5, 16] and nonlinear dynamics [17] that can be exploited for machine learning brought forth this in operando polymerization technique. Although the process is simple and fast, having precise control over the reaction dynamics and the polymerization direction is often hard: unraveling the details of the physical processes that control the growth is key for large-scale electronic implementation. To this end, we investigated the effect of field strength, frequency, electrode gap, and nature of the solvent on the direction and branching of fibers. Additionally, to confirm our observations, we developed a simplified numerical model based on Monte-Carlo simulations to study the reaction dynamics and the growth mechanism. The model uses electrode shape and distance, the composition of the electrolyte, frequency, and voltage applied to compute the features of the polymer network. We show that the experimentally grown networks and simulation results exert the same properties under the same specified experimental conditions. Therefore, the model captures the most relevant aspects of the growth and stands as a suitable tool for designing polymer-based synaptic networks.

2 Methods

Before any deposition, the substrates underwent 10 min of plasma cleaning. 50 nm Au electrodes were patterned glass substrates with a 3 nm Cr adhesion layer by photolithography and wet-etching using Standard Etchant Gold and Standard Etchant Chromium. The photo-resist used for gold lithography was nLoF 2000. Passivation of the electrodes was obtained by SU-8 masking, leaving the tips exposed to the electrolyte. As a next step, the devices were gently rinsed in ethanol and baked at 110 °C for 10 min. Fibers of the conductive poly-3,4-ethylenedioxythiophene doped with hexafluorophosphate (PEDOT:PF6) were prepared by AC electropolymerization in an electrolyte solution under AC signals with an HP 8114A pulse generator between the gold electrodes. The electrolyte solution contained acetonitrile, sulfolane, or a mixture of the two as the solvent, with 1 mM TBAPF6 as the salt, and 50 mM EDOT as the monomer. The electrochemical impedance spectroscopy and cyclic voltammetry measurement were conducted with Autolab PGSTAT302N. The impedance measurement was carried out by using a sinusoidal signal with VRMS: 20 mV. The simulated electrochemical cell used in the experiment is modeled with a box size of 250 unit², electrodes with a width of 40 pixels, and electrode spacing of 15 or 25 pixels. The time step unit equivalent of the simulations is 0.78 ms. Voltage measurements at the load resistor (1 MΩ) were carried out with an oscilloscope and were simulated in LTSpice.

3 Results and discussion

3.1 Physical parameters influencing the growth

The system in exam is an electrolytic solution containing a monomer 3,4-ethylenedioxythiophene (EDOT) in concentration [M], and salt in concentration [S]. As for the salt, we use tetrabutylammonium hexafluorophosphate (TBAPF₆), but other electrolytes can be used as dopants, e.g. LiClO₄ or poly(sodium4-styrenesulfonate). The solvents used are acetonitrile, sulfolene, or a mixture of those. The solution immerses the area between two metal plates. The electrodes are connected to a pulse generator: a square-wave signal $V(t)$ of period T , variable duty cycle, and amplitude switching from V_0 to $-V_0$ is applied across the plates. Several works have reported similar scenarios [13, 18, 19]. The AC signal triggers the branching of polymeric fibers out of both of the electrodes, that grow following the electric field lines until they bridge and connect the two electrodes. To understand the activity of monomers in the growth process, an equivalent circuit model is built (Fig. 1a). The electrode–electrolyte interfaces are represented by Randles circuits where the resistive component captures the charge transfer of the monomer oxidation into a radical cation by losing one electron at the interface [20, 21]. The bulk solution is modeled with a resistor. To verify the validity of this model, a corresponding experiment is carried out in combination with the actual growth process, by combining a pulse generator connected to the electrochemical cell with two probes, and the impedance spectroscopy measurement connected to the electrochemical cell. To minimize the voltage needed for the electropolymerization, firstly a threshold voltage for polymerization initiation is obtained by shrinking the amplitude of the voltage to a small range and confirming the smallest voltage for growth with the pulse generator: at 2.5 V the fiber first branches out from the electrodes and starts advancing in the solution. Then, the voltage amplitude is further decreased to 2 V: the fibers grow progressively from the protrusion. This is a second threshold since with lower voltages the growth process stops. These two threshold voltages are employed as a DC offset voltage in impedance spectroscopy measurement in a frequency range that is compatible with the growth

Fig. 1 Impedance characterization during the growth. **a** Equivalent circuit model. **b** Nyquist plots of a process with 2.5 V offset and a process with 2.0 V offset. **c** Corresponding Bode plots

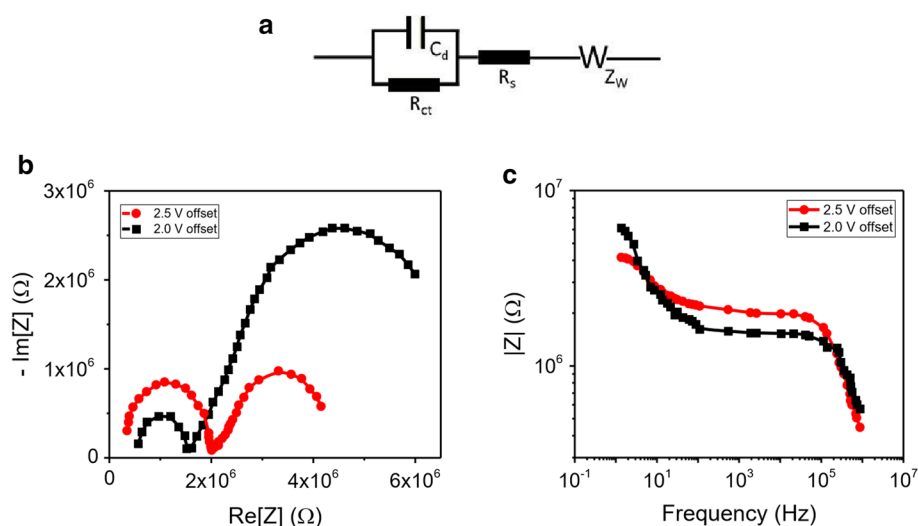
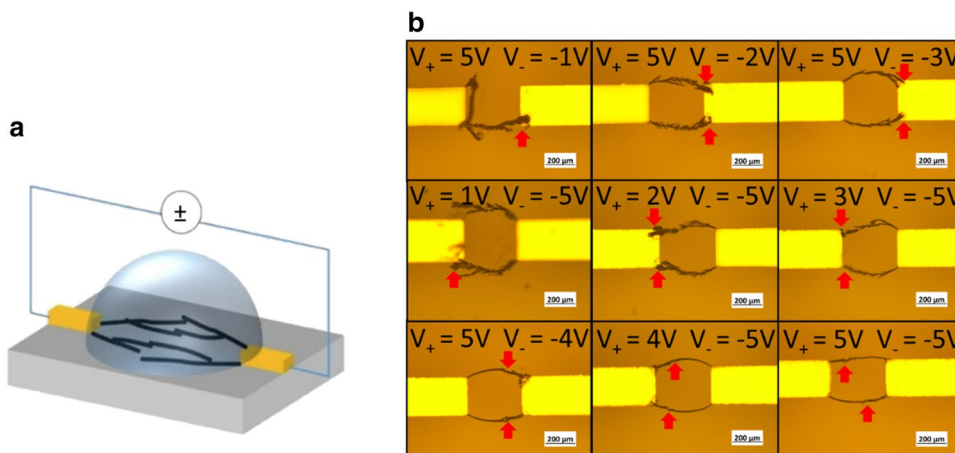


(Fig. 1b–c). The corresponding Nyquist plots are obtained after impedance measurement (Fig. 1b). The semicircle in high frequency is the feature of the simplified Randles circuit. The shift of this semicircle on the x-axis from the origin can be taken as the solution resistance. As shown in Fig. 1b, the 45° slope followed by a semicircle in the low-frequency range can be modeled as the finite length Warburg element [21].

The growth process is established with the drift generated by the alternating voltage, as shown in Fig. 2a. On the positive electrode, anions accumulate and the monomer gets oxidized, while the cations drift to the other electrode. When the polarity changes, the process is reversed. For a duty cycle of 50% and equivalent amplitude for the two half-cycles, the process is expected to be symmetric. To elucidate the mechanism, we grew fibers in asymmetric conditions i.e. changing the amplitudes, and using a frequency of 8 Hz and a duty cycle of 50% (Fig. 2b). The connection of fibers coming from the two electrodes indicates the preferential direction of the growth (arrows in Fig. 2b). By setting the voltage at the counter electrode under or over a certain value, it is possible to guide the fiber growth in preferential directions. In particular, we observed that the fiber grows unidirectional from the working electrode to the counter electrode and attaches to the latter one when the bias of the counter electrode is lower than 3 V. Additionally when the biases of the two electrodes are all above 3 V, multiple fibers grow from the paired electrodes and connect at some point in the gap. The connecting points of the two fibers shift from the gap middle towards one electrode according to the degree of peak asymmetry to the horizontal axis. The differentiation between those two growing modes arises when the smaller bias in the square wave is set to 3 V. This value is close to the threshold oxidation voltage (2.5 V) which is obtained during the equivalent circuit modeling. It is considered as the threshold oxidation potential for such an electropolymerization setup (i.e., acetonitrile with 50 mM EDOT and 1 mM TBAPF6 solution). The overpotential with respect to the theoretical value for EDOT oxidation (1.46 V, as shown in Figure S3) is considered to overcome the energy barriers brought by electrode activation [22], the desolvation of reactants [23], and the charge transfer resistance crossing the electrode–electrolyte

Fig. 2 Direction and dimension of the fibers. **a** The experimental setup used for the growth process consists of two electrodes, a signal generator, and an electrolyte solution containing EDOT monomers. **b** The fibers meet in the gap with a symmetry dictated by the shape of the electrical field in the solution. Arrows: contact points between fibers coming from the two electrodes



interface [24]. When the applied bias on the electrode cannot meet the threshold, the fiber growth on the electrode with a small amplitude is negligible. Therefore, we conclude that asymmetry of the applied signal influences the dynamics of the process, as visible from the different final morphologies (Fig. 2), and therefore can be used for setting a leading seed (electrode) for the growth.

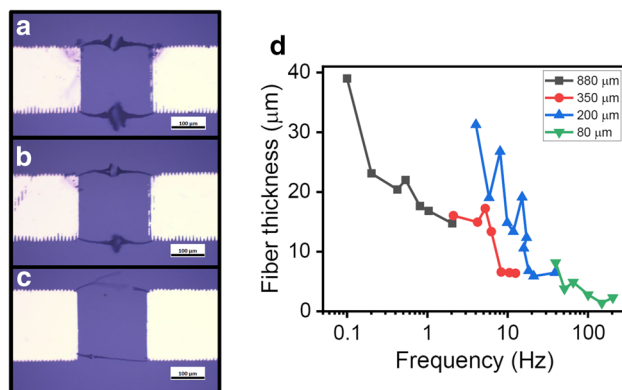
Based on the aforementioned results, the fiber thickness is controlled by varying the electric field strength or limiting the drift time of the charged species, by changing the frequency of the alternating signal (f). We patterned a pair of electrodes by photolithography with defined gaps: 80 μm , 200 μm , 350 μm , or 880 μm , as shown in Fig. 3. This ensures a different field distribution for each of these geometries, although the excitation signal is the same (± 5 V). For the paired electrodes in each gap, the frequency varied from a threshold value above which fibers do not branch out to a small value at which the fibers are thick, which we found to be different for each gap. As summarized in Fig. 3a–c, the thickness of the fibers is following a decreasing trend with increasing frequency. It is possible to describe the action of the alternating signal as a signal of “growth-ON” and “growth-OFF” for each of the two electrodes in the system. During the “growth-ON” time (positive half-cycle), monomers are consumed upon polymer complex formation, which creates a concentration gradient to allow monomers to diffuse to the reaction sites. During the “growth-OFF” time, the diffusion is overcome by the ion motion set into place by the direction change of the ions generated by the electric field. Therefore, the monomer reaction is predominantly governed by half period of the square wave. Additionally, when the growth is stimulated under the same frequency, the fibers grow thicker in the smaller gaps, as in the case of 350 μm and 200 μm (Fig. 3d). Since the amplitude of the applied bias is constant, we conclude that this stems from the strengthened electric field in the smaller spacing. We then tested different solvents to understand their effect on the branching of fibers. We investigated acetonitrile, sulfolane, and their mixtures in different ratios. The amplitude of the AC is kept constant (± 5 V), while the frequencies are chosen for the different conditions (5 Hz for sulfolane, 60 Hz for acetonitrile, and 5 Hz for mixtures to account for their different viscosity).

As shown in Fig. 4a–b, single fibers can be obtained in sulfolane, while multiple branched fibers can be obtained in acetonitrile. When these two solvents are mixed with a ratio of 1:1 or 1:3, only single fibers can be obtained (Fig. 4c–d). When these two solvents are mixed in a ratio of 3:1, single fibers are obtained with few cases in which branching occurs (Fig. 4e–f). Such diversity led us to two major observations. Firstly, the different results could be explained by a different viscosity of the solvent, connected to the diffusion coefficient according to the Stokes–Einstein relation:

$$D = \frac{kT}{6\pi\eta r} \quad (1)$$

where k is the Boltzmann constant, T is the temperature, r is the radius of the particles and η is the solution viscosity. In acetonitrile ($\eta = 0.34$ cP at 300 K), once a concentration gradient is created by consuming monomers upon fiber formation, the fresh monomer can be supplied to the electrode/protrusion quickly from all directions, giving rise to branched fibers. When sulfolane is used instead, ($\eta = 1.00$ cP at 300 K), the supply can be very slow, resulting in the growth of an individual fiber along the direction where the electric field is the strongest. The second observation comes from the shape of the leftover solution in the electrode gap, which is associated with branching uncertainty when acetonitrile and sulfolane are mixed in a 3:1 ratio. As shown in Fig. 4e–f, multiple branches can be found in the sphere shape leftover solution, whereas single fibers are found in a flat leftover solution. We speculate that this difference in the shape of the leftover solution is caused by the evaporation of volatile acetonitrile. As reported elsewhere [25], solvent evaporation

Fig. 3 Fibers grown at different frequencies: 5 Hz (a), 10 Hz (b), and 20 Hz (c). Fiber thickness measured at different electrodes spacings (d)



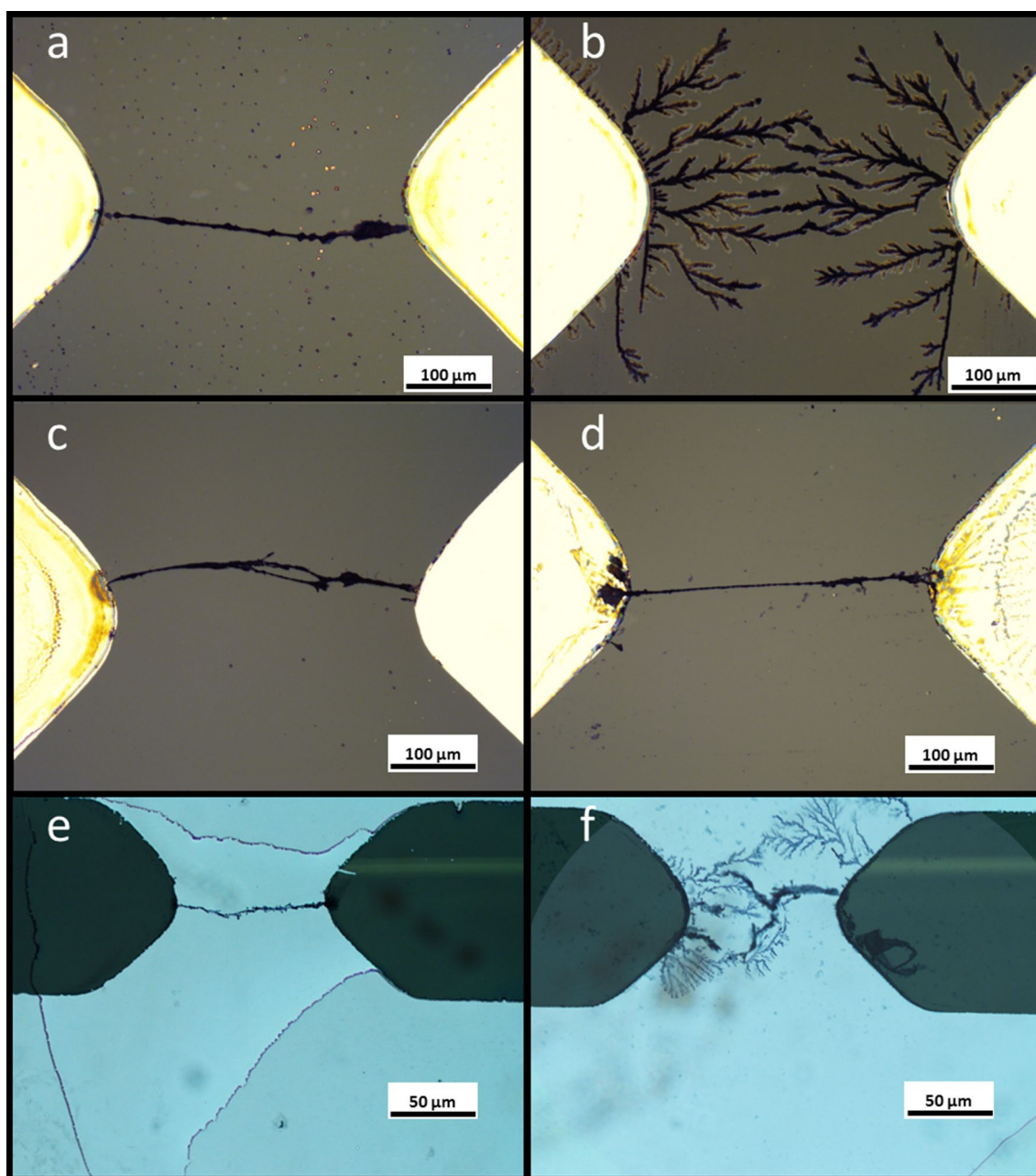


Fig. 4 Microscopic images of fibers grown in (a) sulfolane, b acetonitrile, c acetonitrile:sulfolane = 1:1, d acetonitrile:sulfolane = 1:3, e and f acetonitrile: sulfolane = 3:1. Illustration of the droplets in (e) and (f) were graphically enhanced to increase visibility

establishes a convective flux in the liquid phase and contributes to the single fiber growth. Since a variation in the shape of the leftover solution suggests the uneven mixing of sulfolane in acetonitrile domains, the uncertainty might also be explained by the electro-hydrodynamic flow in multiphase systems [26]. We believe that the suspension of weakly conducting droplets (i.e., acetonitrile dissolved electrolyte) is along or perpendicular to the direction of the electric field in the immiscible weakly conducting solution (i.e., sulfolane dissolved electrolyte) due to the polarization effect. In most cases, acetonitrile evaporates very quickly, the leftover solution is flat and can only employ sulfolane as the solvent, so the formed structure is very similar to that of pure sulfolane. However, in a spherical leftover solution, a certain amount of acetonitrile droplets might be trapped and cannot escape quickly enough from the high viscous sulfolane dominant solution. This uneven distribution of acetonitrile droplets and their polarization results in branching when the fiber formation propagates inside the acetonitrile-dissolved droplets and through the acetonitrile-sulfolane interface.

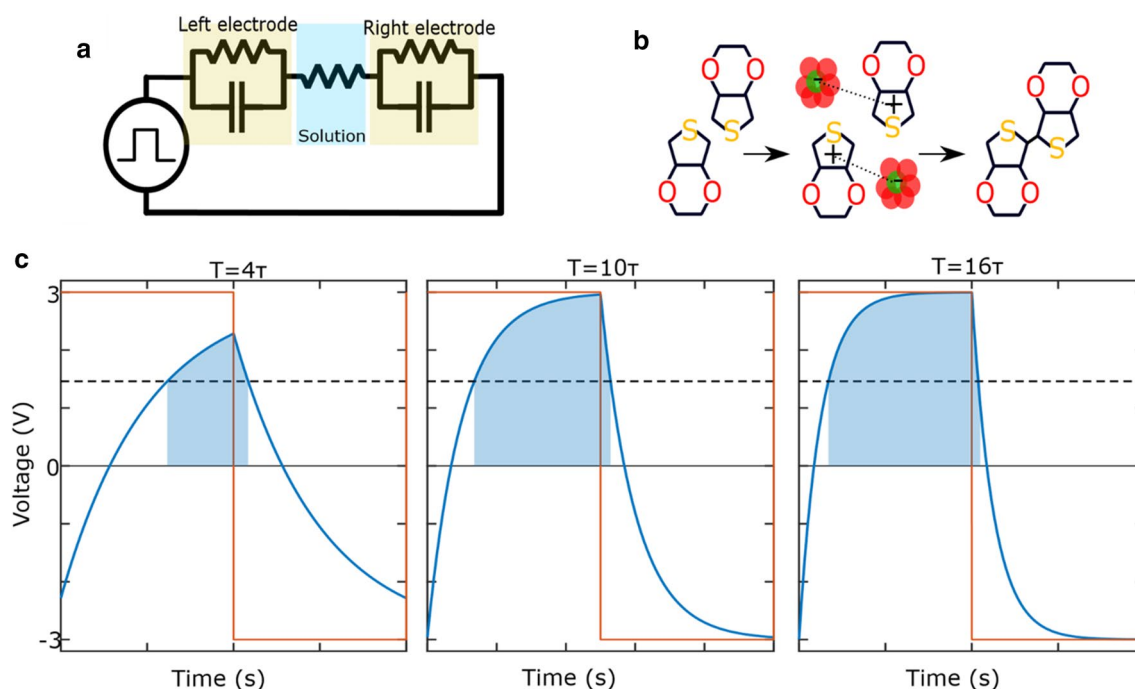


Fig. 5 The equivalent circuit used to model the charge accumulation at the interface (a). The reaction mechanism considered to model the polymerization rate: The monomer is oxidized at the cathode-electrolyte interface, forming a radical monomer cation; Neutralization occurs via an anion. This stabilization process is key for the final conductive state of the polymer: the excess negative charge is given, in fact, by the dopant which determines the final conductivity of the network. Radical-radical reaction leads to the formation of large, insoluble oligomers (b). The voltage transient at the interface (c). The dashed line indicates the oxidation potential, and the blue area is used to calculate the amount of reacting monomers

3.2 Interface description

To make a simplified, yet effective model of the growth, we reduced the electrochemical equivalent of the system to an RC couple for each electrode–electrolyte interface, separated by a resistor, which models the electrolyte (Fig. 5a).

We then validated the model by simulating different experimental configurations. The AC applied voltage is a square wave signal with period T , 50% duty cycle, and amplitude $\pm V_0$. A square wave can be expanded in its Fourier series as:

$$V(t) = \frac{4}{\pi} V_0 \sum_{k=1}^{\infty} \frac{\sin(2\pi(2k-1)\frac{t}{T})}{2k-1} \quad (2)$$

By applying Kirchhoff's voltage law to the circuit in Fig. 5a, $V(t)$ is found to be:

$$V(t) = 2V_i(t) + R_s i(t) \quad (3)$$

where V_i is the voltage drop across the interface and $i(t)$ is the current injected into the system. Applying Kirchhoff's current law, and substituting with the constitutive equations for resistors and capacitors:

$$i(t) = i_{R_i}(t) + i_c(t) = \frac{V_i(t)}{R_i} + C \frac{dV_i(t)}{dt} \quad (4)$$

Therefore, Eq. (3) becomes:

$$V(t) = 2V_i(t) + R_s \left(\frac{V_i(t)}{R_i} + C \frac{dV_i(t)}{dt} \right) \quad (5)$$

which in turn, by defining $\theta = R_s C$ and $\tau = R_s C (2 + \frac{R_s}{R_i})^{-1}$, the previous equation simplifies to:

$$\frac{dV_i(t)}{dt} + \frac{V_i(t)}{\tau} = \frac{V(t)}{\theta} \quad (6)$$

The solution to Eq. (6) is a sequential charge and discharge equation with alternating signs, given by:

$$V_i(t) = \exp\left(-\frac{(t-t_0)}{\tau}\right) \left[V_i(t_0) + \frac{4V_0}{\pi\theta} \int_{t_0}^t \exp\left(\frac{t'-t_0}{\tau}\right) \sum_{k=1}^{\infty} \frac{\sin\left(2\pi(2k-1)\frac{t'}{T}\right)}{2k-1} dt' \right]. \quad (7)$$

After a transient time that depends on the initial charge of the capacitors, the voltage oscillations reach an equilibrium in which the charge accumulated during the positive half-cycle is the same accumulated during the negative one, with the opposite sign. Our model uses the following equilibrium conditions:

- The positive interface voltage accumulated during one half-cycle is equal to the negative voltage accumulated during the following half:

$$V(0) = -V\left(\frac{T}{2}\right) \quad (8)$$

- The solution has periodic boundary conditions:

$$V(0) = V(T) \quad (9)$$

By imposing these conditions on the general formula, the solution at the equilibrium is obtained:

$$V_i(t) = V(t) \left[1 - \Delta \exp\left(-\frac{t}{\tau}\right) \right] \frac{\tau}{\theta} \quad (10)$$

where Δ is a function of the signal's frequency and it is defined as:

$$\Delta = \frac{2}{1 + \exp\left(-\frac{T}{2\tau}\right)} \quad (11)$$

According to the Poisson equation:

$$\rho(x) = \epsilon\epsilon_0 \frac{d^2 V(x)}{dx^2} \quad (12)$$

the time-varying charge accumulation at the interface is described by the charge density $\rho_i(t)$:

$$\rho_i(t) = \epsilon\epsilon_0 \frac{d^2 V_i(x)}{dx^2} \frac{\tau}{\theta} \left(1 - \Delta \exp\left(-\frac{t}{\tau}\right) \right) \quad (13)$$

Considering an exponentially decaying spatial distribution of the potential, as expected in an electrolyte, the voltage can be written as:

$$V(x) = V_0 \exp\left(-\frac{x}{\lambda}\right) \quad (14)$$

where λ is the (Debye) screening length, defined as

$$\lambda = \sqrt{\frac{\epsilon\epsilon_0 RT}{2000 F^2 [S]}}, \quad (15)$$

with F being the Faraday constant. The charge density at the interface can be written as:

$$\rho_i(t) = \epsilon\epsilon_0 \frac{V(t)}{\lambda^2} \frac{\tau}{\theta} \left(1 - \Delta \exp\left(-\frac{t}{\tau}\right) \right) = \rho_{max} \left(1 - \Delta \exp\left(-\frac{t}{\tau}\right) \right) \quad (16)$$

By considering that $V(t) = V_0$ or $V(t) = -V_0$ depending on the polarity of the pulse, and generalizing for a periodic function, Eq. (16) becomes:

$$\rho_i(t) = \rho_{max} \begin{cases} 1 - \Delta \exp\left(-n \frac{t}{\tau}\right), & \text{if } 0 < t < \frac{T}{2} \\ \Delta \exp\left(-n \frac{t - \frac{T}{2}}{\tau}\right) - 1, & \text{if } \frac{T}{2} < t < T \end{cases} \quad (17)$$

with n being an integer number. Figure 5a shows the electrochemical equivalent of the system, that we described with two electrode–electrolyte interfaces represented by RC parallels, while the electrolyte solution with a resistance R_s . Figure S1 proves the validity of this model by comparing the transient analysis to a Spice simulation. Upon application of $V(t)$, the time-dependent voltage $V_i(t)$ at the electrode/solution interface is described by the following periodic equation:

$$V_i(t) = V_0 \frac{\tau}{\theta} \begin{cases} 1 - \Delta \exp\left(-n \frac{t}{\tau}\right), & \text{if } 0 < t < \frac{T}{2} \\ \Delta \exp\left(-n \frac{t - \frac{T}{2}}{\tau}\right) - 1, & \text{if } \frac{T}{2} < t < T \end{cases} \quad (18)$$

Notice that the form is the same as the charge density. A complete description of the reaction mechanism of electropolymerization should include the dimerization of EDOT upon the application of a voltage larger than its oxidation potential V_{ox} ; dimerization is followed by oligomerization, and finally deposition at the interface. Although there is no general agreement on one reaction mechanism, different comprehensive descriptions are found in the literature [18, 27, 28]. All proposed mechanisms have in common, that the monomer is initially oxidized by the oxidation potential and stabilized by a negative counterion. The radical monomer can then further react to form a polymer. From this simple picture, we assume that the reaction proceeds via three steps that occur at the electrode–electrolyte interface or polymer–electrolyte interface (Fig. 5b).

1. Electrochemical oxidation of a monomer M at the cathode–electrolyte interface, forming a radical monomer cation M^+ ;
2. Neutralization of the excess charge M^+ via an anion. This stabilization process is key for the final conductive state of the polymer: the excess negative charge is, in fact, the dopant, and its presence determines the final conductivity and volumetric capacitance of the network.
3. Radical–radical reaction leads to the formation of large, insoluble oligomers

The electrochemical oxidation of the EDOT is the fundamental step to generate the seed for a polymeric fiber. The voltage is expected to be the same along the electrolyte–exposed electrode. Therefore, oxidation can occur at each point of the electrode which is exposed to the electrolyte. On the other hand, we hypothesize that an anion has to neutralize the oxidized complex to generate the polymer. For this reason, both the oxidated monomer and the dopant drift towards the regions where the field is the highest, being the tip of a triangular electrode, or the edges of a rectangular electrode. When neutralization occurs at that point, the seed is established for other components to be transported and attached to it.

The polymer formation dP/dt depends on both the monomer concentration $[M]$ and the anion concentration at the interface $[S_i(t)]$. Hence, it can be described as a second-order polymerization reaction:

$$\frac{dP(t)}{dt} = \frac{d[M(t)^+]}{dt} = \begin{cases} k[M]^2[S_i(t)]^2, & \text{if } V_i > V_{ox} \\ 0, & \text{else} \end{cases} \quad (19)$$

where k is the equilibrium constant. The monomer concentration $[M]$ is assumed to stay constant during electropolymerization. The salt concentration at the interface varies with time and is defined as $[S_i(t)] = \frac{\rho_i(t)}{F}$. The potential at the metal–electrolyte interface has to exceed V_{ox} in order for the reaction to occur. $V_i(t)$ is going to rise above V_{ox} only if $V_0 > V_{ox}$ and if the period is long enough for the interface to charge. During the positive half-cycle, this threshold is reached at $t = t_{th+}$ that is evaluated as:

Table 1 Growth parameters

Parameter	Symbol	Value	Source
Dielectric constant acetonitrile		37.5	[29]
(dis)Charging time constant	τ	1.3 ms	Figure S1
Damping factor	Θ	4.8 ms	Figure S1
Monomer concentration	[M]	50 mM	Experiments
Salt concentration	[S]	1 mM	Experiments
EDOT oxidation potential	V_{ox}	1.46 V	Figure S3
Debye length	λ	6.5 nm	Eq. (15)

$$t_{th+} = \tau \ln \left(\Delta \frac{V_0 \tau}{V_0 \tau - V_{ox} \Theta} \right) \quad (20)$$

Similarly, in the half period with negative polarity, the interface voltage decreases below V_{ox} after a time t_{th-} defined as:

$$t_{th-} = \tau \ln \left(\Delta \frac{V_0 \tau}{V_0 \tau + V_{ox} \Theta} \right) \quad (21)$$

The available time window for the polymer to form is proportional to the integral shown in Fig. 5c, between t_{th+} and t_{th-} . By defining $T_{th} = \frac{T}{2} - (t_{th+} + t_{th-})$, the integral reads:

$$\int_{t_{th+}}^{t_{th-}} [S_i(t)] dt = \frac{\rho_{max}}{F} \left(T_{th} + \tau \Delta \left(e^{-\frac{T}{2\tau}} - e^{-\frac{t_{th+}}{\tau}} - e^{-\frac{t_{th-}}{\tau}} + 1 \right) \right). \quad (22)$$

The circuit parameters are evaluated with LTSpice and reported in Figure S1 and referred to the case of a couple of flat gold electrodes. Plugging Equation (22) into Equation (19) gives the amount of polymer formed in each period. Table 1 reports all the parameters relevant to the description.

Two important comments must be made: i) the reaction never occurs without an applied voltage or a voltage below V_{ox} and ii) an electric field has to support the growth: in fact, bifurcation only happens at the extremities, and never a fiber branches out laterally from existing fibers. $V > V_{ox}$ is a necessary condition but not sufficient for the process to start: if no electric field is built up, the reaction does not occur. This scenario is common during the growth where, while the rate is high at the electrodes extremities due to the high field (tip effect), the polymerization does not occur in the area between two already existing fibers. Here the potential is enough to form M^+ , but $[S_i]$ is too little due to the negligible field (Faraday cage effect). Figure S2 shows the integral value with varying voltage amplitude and pulse frequency.

3.3 Growth modeling

To validate the model, we developed a simulation platform based on the Montecarlo method that captures the following features:

1. the motion of charged species in the liquid;
2. deposition of charged species on the electrode;
3. evolution of electric map due to the modified electrode and time-variant signal.

Figure 6a–b show the schematic representation of the process and the corresponding flow chart. Herein, a 2D box is simulated to model the region of interest (ROI) in the electrolytic environment. We used different geometries (gray shapes) to account for potential shapes of interest for the electrodes (Fig. 6c). The specific number of charged particles (white points) are distributed in the box at random locations.

The potential map in the complete region of interest is evaluated with the boundary conditions of the applied signal onto the electrodes. The particles' motion is evaluated based on the gradient of the electric field and the Brownian motion. A certain probability of being incorporated by the metal or the pre-existing polymeric fiber is associated with the particles touching the electrodes from any of the available directions. In particular, the probability of attachment is considered to be sigmoidal, with the probability value depending on the potential difference between the particle

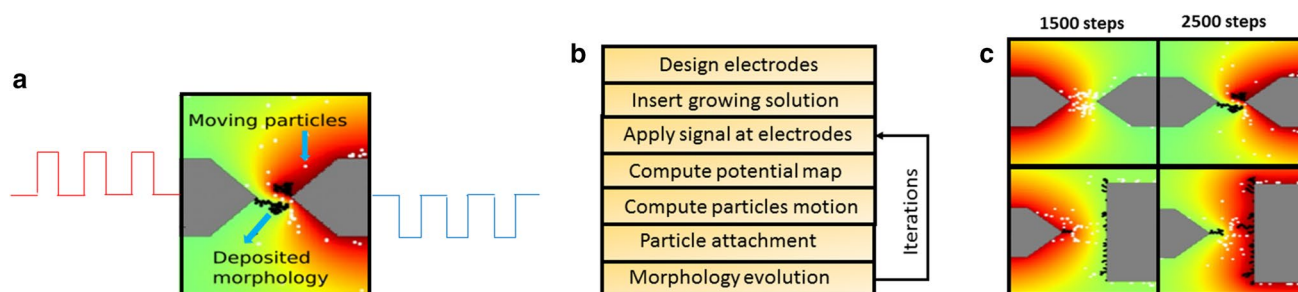
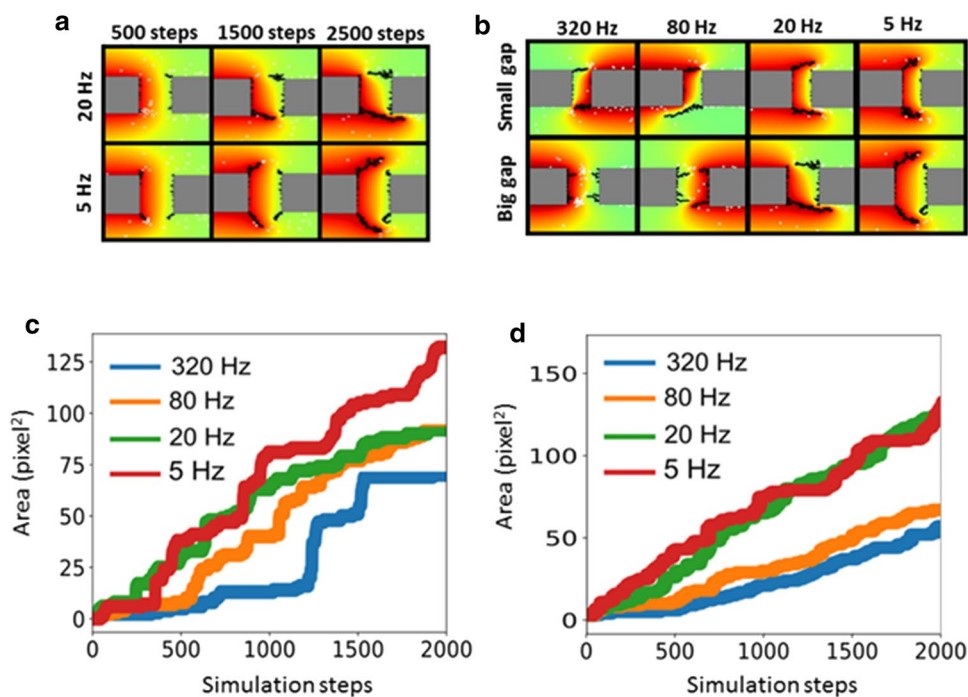


Fig. 6 Schematic representation of the mesoscale modeling for the dendritic growth (a). Flow chart of major steps used in the modeling (b). Modeling results with two V-shaped electrodes and a V-shaped against a flat electrode (c)

Fig. 7 Modeling of the dendritic growth process at 5 Hz and 20 Hz at different simulation steps (a). Frequency sweep of the growth in geometries with big and small electrode gap (b). Area occupied by the pixels associated with the fibers for different frequencies in the case of small (c) and big (d) electrode gap



and the electrochemical double layer. Therefore, the attached morphologies (shown in black), are considered integral parts of electrodes to compute the electrical field distribution in the successive simulation steps. While the structure keeps evolving, the amount of deposited material is calculated over time. Figure 6c shows the growth of morphology with V-shaped and square electrodes. For a significant time (1500 simulation time steps), there is no growth on the V-shaped electrodes. The charged particles are dragged near the tips of the electrodes. Interestingly, the charged particles move towards the center of the electrodes and converge near the tip. From that point, the growth initiates, and a dendritic morphology from the tip of the electrode is obtained. The density of the particles continues to rise in the centers of the electrodes. In the case of a tip electrode on the left and a flat electrode on the right, at $t = 1500$ steps, there is a linear-shaped growth at the left electrode which moves from the tip of the electrode towards the flat electrode. On the other hand, at the right electrode, a quasi-uniform growth is established on the flat electrode. The particle dispersion also forms a contour around the tip, migrating from the tip towards the central part of the flat electrode. At $t = 2500$ steps, the density of the deposited morphologies at both electrodes increases. On the tip electrode, the evolving dendritic morphology starts branching towards the flat electrode, following the field lines. Next, we studied the growth process by analyzing two important parameters: electrode spacing and applied signal frequency. Figure 7a shows the images of dendritic morphologies at 20 Hz and 5 Hz respectively, exerting distinct characteristics, as already described in the experimental equivalent. The morphology features a thinner growth for the case of signals with higher frequencies, while it possesses thick dense morphology with branching behavior at lower frequencies. This property is preserved for the whole duration of the growth (2500 steps).

The growth for both frequencies occurs at the tips, and dendritic morphology advances towards the opposite electrode. In the case of higher frequency, the morphology shows more directionality towards the opposite electrode, and a thinner dendritic structure advances towards the other electrode. In the case of lower frequency growth, the morphology possesses a transversal component and high divergence leading to more dense morphology. Figure 7b shows the morphologies at variable frequencies for two different electrode spacings (15 pixels and 25 pixels). An increase in the period promotes random walks. Thus, instead of an ideal thin line formed at high frequencies, a broad thicker dendritic morphology is obtained in the configurations with longer stimulation periods. Figure 7c and Fig. 7d show the variations of deposited material as a function of the time steps for small and big electrode gap, respectively. It is known that the capacitance of films composed of CPs is directly proportional to their area. Our model shows that lower frequencies result in denser films which should in turn translate into larger capacitances, in agreement with previous observations [5]. The growth process is slower for high frequencies (320 Hz) and becomes faster for lower frequencies. Here, the probability to touch thin wires by the particles is lower, and hence the dendritic growth is kinetically slower with high signal frequency. Another reason is that for a high switching rate of the voltage, fewer particles have the chance to reach far regions before being pulled back to the other electrode.

4 Conclusions

In this paper, we looked at how organic dendritic networks made of the semiconductor PEDOT:PF6 grow by varying different physical parameters, and studied their different emerging features. We revealed the effects of field strength, asymmetry of the electrical stimuli, the geometry of the gold pads, electrode pitch, and charging and discharging times on the size, branching, and direction of the fibers. We then developed a simplified model to describe the electrode–electrolyte interface. This model maps the device pattern and foresees the spatial–temporal evolution of the growth by computing the electrical field distribution at every iteration, taking into account the distortions introduced by the newborn polymeric seeds or fibers. With this model, we were able to validate the main features of the growth with good precision and therefore confirm our hypotheses. To unlock the full potential of the technique, and therefore of the model, a generalized study on the effect of AC polymerization should be carried out on multiple electrodes and extended on more complex geometries such as pillars, micro-ridges, and micro-grooves, in order to account for the possibility of three-dimensional growth. In the future, the mentioned settings could be applied to the design of conductive polymeric scaffolds with adjustable neuromorphic properties.

Author contributions GC, MC, YG, and AK provided equal contributions to the work. All authors read and approved the final manuscript.

Funding Open Access funding enabled and organized by Projekt DEAL. The authors acknowledge funding from the Hector Fellow Academy (30000619), the Volkswagen Stiftung (96574), and ERC-CoG IONOS (#773228).

Data availability The datasets generated during and/or analyzed during the current study are available from the corresponding author on reasonable request.

Code availability The codes used during the current study are available from the corresponding author upon reasonable request.

Declarations

Competing interests The authors declare no competing interests.

Open Access This article is licensed under a Creative Commons Attribution 4.0 International License, which permits use, sharing, adaptation, distribution and reproduction in any medium or format, as long as you give appropriate credit to the original author(s) and the source, provide a link to the Creative Commons licence, and indicate if changes were made. The images or other third party material in this article are included in the article's Creative Commons licence, unless indicated otherwise in a credit line to the material. If material is not included in the article's Creative Commons licence and your intended use is not permitted by statutory regulation or exceeds the permitted use, you will need to obtain permission directly from the copyright holder. To view a copy of this licence, visit <http://creativecommons.org/licenses/by/4.0/>.

References

1. van de Burgt, Y, Melianas, A, Keene, S et al. Organic electronics for neuromorphic computing. *Nat Electron*. 2018. <https://doi.org/10.1038/s41928-018-0103-3>
2. Gumyusenge A, et al. Materials Strategies for Organic Neuromorphic Devices. *Annual Review of Materials Research*. 2021. <https://doi.org/10.1146/annurev-matsci-080619-111402>
3. Van Doremaele ERW, Gkoupidenis P, Van De Burgt Y. Towards organic neuromorphic devices for adaptive sensing and novel computing paradigms in bioelectronics. *J Mater Chem C*. 2019. <https://doi.org/10.1039/c9tc03247a>.
4. Kim M, et al. Emerging materials for neuromorphic devices and systems. *Iscience*. 2020. <https://doi.org/10.1016/j.isci.2020.101846>
5. Cucchi M, Kleemann H, Tseng H, et al. Directed growth of dendritic polymer networks for organic electrochemical transistors and artificial synapses. *Adv Electron Mater*. 2021. <https://doi.org/10.1002/aelm.202100586>.
6. Cucchi M, Gruener C, Petrauskas L, et al. Reservoir computing with biocompatible organic electrochemical networks for brain-inspired biosignal classification. *Sci Adv*. 2021. <https://doi.org/10.1126/sciadv.abh0693>.
7. Seki Y, Takahashi M, Takashiri M. Effects of different electrolytes and film thicknesses on structural and thermoelectric properties of electropolymerized poly(3,4-ethylenedioxythiophene) films. *RSC Adv*. 2019. <https://doi.org/10.1039/c9ra02310k>.
8. Jiang H, Wu W, Chang Z, et al. In situ polymerization of PEDOT:PSS films based on EMI-TFSI and the analysis of electrochromic performance. *E-Polymers*. 2021. <https://doi.org/10.1515/epoly-2021-0073>.
9. Yuan C, Guo S, Wang S, et al. Electropolymerization polyoxometalate (POM)-doped pedot film electrodes with mastoid microstructure and its application in dye-sensitized solar cells (DSSCs). *Ind Eng Chem Res*. 2013. <https://doi.org/10.1021/ie302845z>.
10. Benoudjit A, Bader MM, Wan Salim WWA. Study of electropolymerized PEDOT:PSS transducers for application as electrochemical sensors in aqueous media. *Sens Bio-Sensing Res*. 2018. <https://doi.org/10.1016/j.sbsr.2018.01.001>.
11. Murbach JM, Currin S, Widener A, et al. In situ electrochemical polymerization of poly(3,4-ethylenedioxythiophene) (PEDOT) for peripheral nerve interfaces. *MRS Commun*. 2018. <https://doi.org/10.1557/mrc.2018.138>.
12. Sessolo M, Khodagholy D, Rivnay J, et al. Easy-to-fabricate conducting polymer microelectrode arrays. *Adv Mater*. 2013. <https://doi.org/10.1002/adma.201204322>.
13. Gerasimov JY, Gabrielson R, Forchheimer R, et al. An evolvable organic electrochemical transistor for neuromorphic applications. *Adv Sci*. 2019. <https://doi.org/10.1002/advs.201801339>.
14. Gerasimov JY, Zhao D, Sultana A, et al. A biomimetic evolvable organic electrochemical transistor. *Adv Electron Mater*. 2021. <https://doi.org/10.1002/aelm.202001126>.
15. Liu J, et al. Pathways for practical high-energy long-cycling lithium metal batteries. *Nat Energy*. 2019. <https://doi.org/10.1038/s41560-019-0338-x>
16. Janzakova K, Kumar A, Ghazal M, et al. Analog programming of conducting-polymer dendritic interconnections and control of their morphology. *Nat Commun*. 2021. <https://doi.org/10.1038/s41467-021-27274-9>.
17. Petrauskas L, Cucchi M, Grüner C, et al. Nonlinear behavior of dendritic polymer networks for reservoir computing. *Adv Electron Mater*. 2022. <https://doi.org/10.1002/aelm.202100330>.
18. Koizumi Y, Shida N, Ohira M, et al. Electropolymerization on wireless electrodes towards conducting polymer microfibre networks. *Nat Commun*. 2016. <https://doi.org/10.1038/ncomms10404>.
19. Eickenscheidt M, Singler E, Stieglitz T. Pulsed electropolymerization of PEDOT enabling controlled branching. *Polym J*. 2019. <https://doi.org/10.1038/s41428-019-0213-4>.
20. Tamburri E, Orlanducci S, Toschi F, et al. Growth mechanisms, morphology, and electroactivity of PEDOT layers produced by electrochemical routes in aqueous medium. *Synth Met*. 2009. <https://doi.org/10.1016/j.synthmet.2008.10.014>.
21. Politi S, Tomellini M. Kinetics of island growth in the framework of “planar diffusion zones” and “3D nucleation and growth” models for electrodeposition. *J Solid State Electrochem*. 2018. <https://doi.org/10.1007/s10008-018-4011-2>.
22. Limon-Petersen JG, Streeter I, Rees NV, Compton RG. Quantitative voltammetry in weakly supported media: effects of the applied overpotential and supporting electrolyte concentration on the one electron oxidation of ferrocene in acetonitrile. *J Phys Chem C*. 2009. <https://doi.org/10.1021/jp809302m>.
23. Momeni M, Wren JC. A mechanistic model for oxide growth and dissolution during corrosion of Cr-containing alloys. *Faraday Discuss*. 2015. <https://doi.org/10.1039/c4fd00244j>.
24. Elumalai P, Vasan HN, Munichandraiah N. A note on overpotential dependence of AC impedance data. *J Solid State Electrochem*. 1999. <https://doi.org/10.1007/s100080050183>.
25. Kannan B, Williams DE, Khoshmanesh K, et al. The electrochemical growth of conducting polymer “nanowires.” *J Electroanal Chem*. 2012. <https://doi.org/10.1016/j.jelechem.2012.01.022>.
26. Lin Y, Skjetne P, Carlson A. A phase field model for multiphase electro-hydrodynamic flow. *Int J Multiph Flow*. 2012;45:1–11. <https://doi.org/10.1016/j.ijmultiphaseflow.2012.04.002>.
27. Zhou Y, Shida N, Koizumi Y, et al. Template-free perpendicular growth of a poly(3,4-ethylenedioxythiophene) fiber array by bipolar electrolisis under an iterative potential application. *J Mater Chem C*. 2019;7:14745–51. <https://doi.org/10.1039/C9TC04743C>.
28. Ohira M, Koizumi Y, Nishiyama H, et al. (2016) Synthesis of linear PEDOT fibers by AC-bipolar electropolymerization in a micro-space. *Polym J*. 2017;49(49):163–7. <https://doi.org/10.1038/pj.2016.100>.
29. Gagliardi LG, Castells CB, Ràfols C, et al. Static dielectric constants of acetonitrile/water mixtures at different temperatures and debye-hückel A and a0B parameters for activity coefficients. *J Chem Eng Data*. 2007;52:1103–7. https://doi.org/10.1021/JE700055P/SUPPL_FILE/JE700055P-FILE002.PDF.